Available online at www.sciencedirect.com
SCIENCE DIRECT®
ELSEVIER
Icarus 168 (2004) 186–200
ICARUS
www.elsevier.com/locate/icarus

Water production and release in Comet 153P/Ikeya–Zhang (C/2002 C1): accurate rotational temperature retrievals from hot-band lines near 2.9-μm

Neil Dello Russo,[a,b,*] Michael A. DiSanti,[c] Karen Magee-Sauer,[d] Erika L. Gibb,[e] Michael J. Mumma,[f] Robert J. Barber,[g] and Jonathan Tennyson [g]

[a] *Department of Physics, The Catholic University of America, Washington, DC 20064, USA*
[b] *Laboratory for Extraterrestrial Physics, NASA Goddard Space Flight Center Code 690.2, Greenbelt, MD 20771, USA*
[c] *Laboratory for Extraterrestrial Physics, NASA Goddard Space Flight Center Code 693, Greenbelt, MD 20771, USA*
[d] *Department of Chemistry and Physics, Rowan University, Glassboro, NJ 08028, USA*
[e] *NAS–NRC, Laboratory for Extraterrestrial Physics, NASA Goddard Space Flight Center Code 690.2, Greenbelt, MD 20771, USA*
[f] *Laboratory for Extraterrestrial Physics, NASA Goddard Space Flight Center Code 690, Greenbelt, MD 20771, USA*
[g] *Department of Physics and Astronomy, University College London, Gower Street, London, WC1E 6BT, UK*

Received 6 January 2003; revised 21 October 2003

Abstract

Multiple non-resonance fluorescence lines of water (H_2O) were detected in Comet 153/P Ikeya–Zhang (2002 C1) between UT 2002 March 21.9 ($R_h = 0.51$ AU) and April 13.9 ($R_h = 0.78$ AU), using the Cryogenic Echelle Spectrometer (CSHELL) at the NASA Infrared Telescope Facility. Analysis of 2.9-μm water lines enabled accurate determination of rotational temperatures on three dates. The derived H_2O rotational temperatures were 138^{+6}_{-5}, 141^{+10}_{-9}, and 94 ± 3 K on UT 2002 March 22.0, March 23.0, and April 13.8, respectively. Water production rates were retrieved from spectral lines measured in nineteen separate grating settings over seven observing periods. The derived heliocentric dependence of the water production rate was $Q = (9.2 \pm 1.1) \times 10^{28} [R_h^{(-3.21 \pm 0.26)}]$ molecules s^{-1}. The spatial distribution of H_2O in the coma was consistent with its release directly from the nucleus (as a native source) on all dates.
© 2003 Elsevier Inc. All rights reserved.

Keywords: Comets; Ikeya–Zhang; Infrared; Spectroscopy; Water

1. Introduction

Water is the dominant ice in most (perhaps all) comets, and its sublimation controls the release of other volatiles within 3–4 AU of the Sun. For this reason, the volatile activity of a comet and the abundances of minor species are often expressed relative to H_2O production. At greater distances, more volatile species such as CO may control a comet's activity (Senay and Jewitt, 1994; Crovisier et al., 1995; Biver et al., 1996), and water is then likely released primarily from a distributed source of icy grains (A'Hearn et al., 1984). An accurate determination of cometary water abundances is key to understanding the volatile fraction in comets.

Water production rates in comets can be inferred through detection of its photodissociation products. However, these can also be produced from other parents, and all indirect methods require modeling assumptions to relate the production of the measured species to that of water. Although detection of vibrational and rotational emission from water vapor in comets is readily achieved at airborne altitudes (Mumma et al., 1986) and from space (Combes et al., 1988; Crovisier et al., 1997, 1999; Chiu et al., 2001; Lecacheux et al., 2003), airborne observatories present limited observing opportunities while space observatories have limited lifetimes and usually are subject to sun-avoidance constraints. For these reasons, a general method for direct detection of water from the ground is highly desirable. Ground-based searches for H_2O at radio wavelengths have generally not been successful. The 6_{16}–5_{23} rotational line of water at $\lambda = 1.35$ cm was marginally detected in Comet Hale–Bopp from the ground (Bird et al., 1999). However, this single transition is very weak, and it is also sensitive to the assumed excitation temperature, making the production rate determination uncertain.

* Corresponding author.
E-mail address: ysndr@lepvax.gsfc.nasa.gov (N. Dello Russo).

0019-1035/$ – see front matter © 2003 Elsevier Inc. All rights reserved.
doi:10.1016/j.icarus.2003.11.004

At present, targeting water lines from the ground at infrared wavelengths is the best direct method for constraining water production rates, since in general multiple lines can be observed. Severe extinction by atmospheric water makes detection of cometary H_2O emissions in the fundamental bands problematic from ground-based observatories—these strong transitions terminate in the ground vibrational level which is highly populated in Earth's atmosphere, causing absorption of the incident photons. To avoid such extinction, we target lines in the weaker non-resonance fluorescence bands (hot-bands). Direct absorption of sunlight excites molecules from the lowest vibrational level (000) to a higher vibrational level, followed by cascade into an intermediate level that is not significantly populated in the atmosphere (Crovisier, 1984; Mumma et al., 1995; Dello Russo et al., 2000). The terrestrial atmosphere is generally transparent to these cometary water emissions, and no specific Doppler-shift is needed to observe these hot-band lines.

The first ground-based detections of H_2O in comets were obtained in C/1991 T2 Shoemaker–Levy and 6P/d'Arrest, and in C/1996 B2 Hyakutake using the $\nu_1 + \nu_2 + \nu_3 - \nu_1$ (111–100) and $2\nu_2 + \nu_3 - \nu_2$ (021–010) vibrational hot-bands near 2-μm (Mumma et al., 1995, 1996; Dello Russo et al., 2002a). A survey of the (1–0) band of CO near 4.7-μm in Hyakutake revealed new strong emissions that were identified as non-resonance fluorescence from the $\nu_1 - \nu_2$ (100–010) and $\nu_3 - \nu_2$ (001–010) hot-bands of H_2O (Mumma et al., 1996; Dello Russo et al., 2002a). Since H_2O and CO can be sampled simultaneously near 4.7-μm, these hot-bands have been preferentially targeted to determine water production rates in recent comets (e.g., C/1995 O1 Hale–Bopp (Weaver et al., 1999a; Dello Russo et al., 2000), 21P/Giacobini–Zinner (Weaver et al., 1999b; Mumma et al., 2000), C/1999 H1 Lee (Mumma et al., 2001a), and C/1999 S4 LINEAR (Mumma et al., 2001b)). The detection and quantification of water production in comets is now routinely accomplished through high-resolution infrared spectroscopy at ground-based observatories.

Although the 2, 4.7, and 5-μm spectral regions have been important for studying H_2O production in comets, other spectral regions also contain water hot-bands. Hot-band emission from H_2O was first detected near 2.66 μm in high-dispersion airborne infrared spectra of Comet Halley (Weaver et al., 1986) and in Comet C/1986 P1 Wilson (Larson et al., 1989). Later, hot-band lines were detected in Comets Hale–Bopp and 103P/Hartley 2 with ISO (Crovisier et al., 1997, 1999). Ground-based infrared observations of Comets Halley and Wilson indicated the presence of excess flux near 2.8-μm that was not due to water fundamental bands (Tokunaga et al., 1987; Brooke et al., 1989). It was later surmised that lines from water hot-bands could significantly contribute to this feature (Bockelée-Morvan and Crovisier, 1989). The presence of water hot-band emission in the 2.9–3.0-μm region was confirmed in high-dispersion spectra of Comet C/1999 H1 Lee and later comets (cf. Magee-Sauer et al., 2000).

Here, we report a detailed study of water production and release in Comet 153P/Ikeya–Zhang (C/2002 C1; hereafter Ikeya–Zhang). Preliminary results for water production rates in Ikeya–Zhang on UT April 13.8 were reported by Dello Russo et al. (2002b). In addition to water hot-band lines near 4.7 and 5.0-μm, we detected emission lines from at least four hot-bands near 2.9-μm. We developed temperature-dependent fluorescence models for seven hot-bands near 2.9-μm and applied them to this data set, enabling the accurate determination of H_2O rotational temperatures and production rates in Comet Ikeya–Zhang.

2. Observations and data analysis

We observed Comet Ikeya–Zhang with the cryogenic echelle spectrometer (CSHELL) at the NASA Infrared Telescope Facility on Mauna Kea, Hawaii (Greene et al., 1993). Multiple ro-vibrational lines from at least six water hot-bands were detected during seven observing periods between UT 2002 March 21.9 ($R_h = 0.51$ AU) and April 13.9 ($R_h = 0.78$ AU) (Table 1).

CSHELL has a 256 × 256 pixel InSb array detector with a pixel size of $0.2'' \times 0.2''$, and provides spatial coverage along the $30''$ long slit which we oriented east–west. A $1''$ wide slit was used for our comet observations leading to a spectral resolving power $\nu/\Delta\nu \sim 2 \times 10^4$. At each grating setting, cometary data were acquired using a sequence of four scans (source, sky, sky, source). For sky spectra the telescope was nodded either on or off the chip, providing sky cancellation via pixel-by-pixel subtraction (Table 1). For off-chip nodding, the source frame is centered on the comet and the sky frame is nodded 2 arc-min perpendicular to the slit.

Table 1
Log of Comet Ikeya–Zhang H_2O observations

Setting[a]	UT date 2002	UT time	R_h (AU)	Δ (AU)	Δ-dot (km s^{-1})	Time on source (s)	Nod[b]
2149.3	21 Mar	20:38	0.5117	0.7632	−32.24	240	off
3452.3	22 Mar	00:31	0.5123	0.7602	−31.77	120	off
2137.7	22 Mar	00:40	0.5123	0.7601	−31.75	120	off
2149.3	22 Mar	20:34	0.5155	0.7450	−31.58	60	off
2004.9	22 Mar	21:03	0.5156	0.7446	−31.53	120	off
3452.3	23 Mar	00:17	0.5162	0.7422	−31.12	120	off
2153.1	27 Mar	19:35	0.5492	0.6609	−27.60	60	off
2153.1	10 Apr	18:29	0.7315	0.4905	−15.49	240	on
2153.1	10 Apr	18:38	0.7316	0.4905	−15.48	120	off
2137.7	10 Apr	19:10	0.7320	0.4903	−15.43	480	on
2153.4	11 Apr	19:50	0.7482	0.4815	−14.57	240	on
2153.4	11 Apr	21:32	0.7493	0.4805	−14.30	240	on
2152.9	11 Apr	21:52	0.7495	0.4804	−14.27	240	on
2152.9	12 Apr	17:48	0.7628	0.4740	−13.98	240	on
2137.7	12 Apr	21:25	0.7645	0.4728	−13.63	240	on
2152.9	12 Apr	21:48	0.7655	0.4727	−13.59	240	on
2152.9	13 Apr	17:33	0.7787	0.4663	−13.22	240	on
3452.3	13 Apr	18:45	0.7795	0.4659	−13.12	480	on
2137.7	13 Apr	20:10	0.7805	0.4655	−12.98	240	on

[a] Central wavenumber (cm^{-1}) of the grating setting.
[b] The telescope nod, either on- or off-chip (see text).

For on-chip nodding, the source and sky frames are taken in positions approximately one-quarter the distance from the top and bottom of the slit respectively (15″ nod along the slit). On-chip nodding allows more time on source to be obtained at the expense of spatial coverage. Flat-fields and dark frames were obtained following each scan sequence. For each grating setting, spectra of infrared standard stars were obtained through a 4″ wide slit for absolute flux calibration of the comet spectra.

All observations occurred during daylight when atmospheric seeing is generally poorer and more variable, and tracking non-sidereal objects is more difficult compared to night-time observations since the autoguiding capability of the telescope is not usable. Images of the comet were taken before and after each sequence of scans through a circular variable filter to assess cometary drift and to update telescope-tracking rates as needed. De-focusing can occur if sunlight strikes the telescope structure, so the focus was also checked and updated regularly using a star close to the comet. Seeing, drift, and de-focusing all affect the measured point-spread-function (PSF) of an object. For our observations, the full width at half maximum (FWHM) of a stellar PSF was typically $\sim 1''$–$2''$ and was generally variable within a single observing period.

The data were processed using algorithms specifically tailored to our comet observations. Application of these has been described in detail elsewhere (Dello Russo et al., 1998, 2000, 2001; Magee-Sauer et al., 1999; DiSanti et al., 2001). Initial processing included flat-fielding and removal of high dark current pixels and cosmic ray hits. Spectral frames were registered such that the spectral dimension fell along rows and the spatial dimension along columns. Spectra can then be extracted over any desired spatial extent and position along the slit (Figs. 1, 2). Atmospheric models were obtained using the Spectrum Synthesis Program (SSP) (Kunde and Maguire, 1974) which accesses the HITRAN-1992 Molecular Data Base (Rothman et al., 1992). SSP models were used to assign wavelength scales to the extracted spectra, and to establish absolute column burdens for each significant absorbing species in the terrestrial atmosphere. The (fully-resolved) model was binned to the instrumental sampling interval, convolved to the resolution of the comet spectrum and normalized to the cometary continuum (Figs. 1, 2).

Volatile emission features were separated from the continuum by subtracting the normalized atmospheric model from the comet spectrum row-by-row, yielding the net cometary molecular emissions still convolved with the atmospheric transmittance function (Fig. 2). The true line flux ($F_{\rm line}$) incident at the top of the terrestrial atmosphere was determined from the observed flux by correcting for the monochromatic transmittance at the Doppler-shifted line position (obtained from the fully-resolved SSP model). The IRTF policy allowing daytime observations, the high spectral resolving power of CSHELL, and the favorable apparition of Comet Ikeya–Zhang, allowed detections of multiple water lines from at least six different hot-bands (Figs. 1, 2).

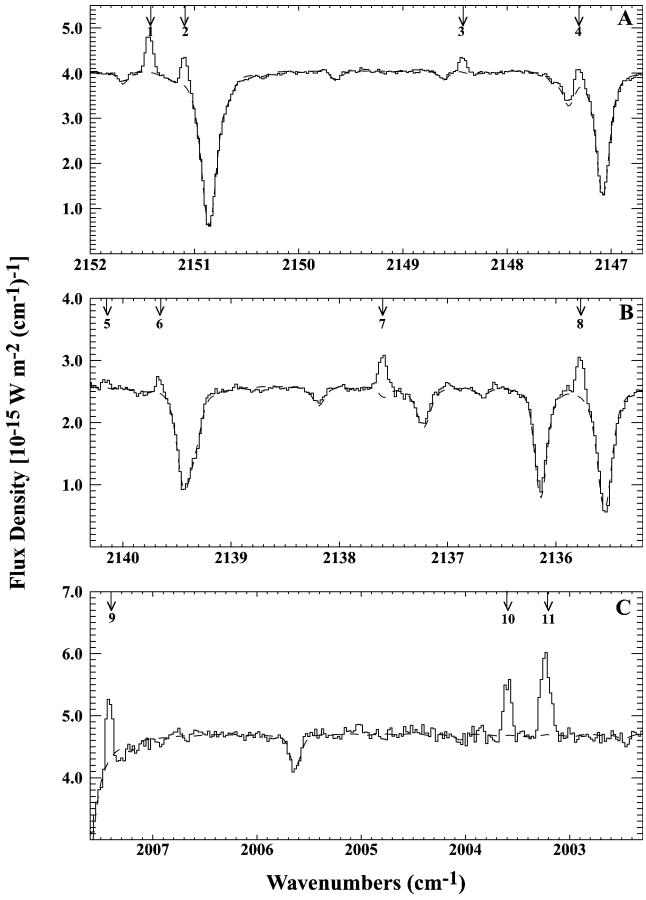

Fig. 1. Detection of 4.7 and 5.0-μm hot-band lines in Comet Ikeya–Zhang. (A) UT 2002 March 21, 20:38. (B) UT 2002 March 22, 00:40. (C) UT 2002 March 22, 21:03. Flux-calibrated spectral extracts $1'' \times 3''$ (5 columns × 15 rows) of Comet Ikeya–Zhang centered on the peak of the gas emission (solid curves). Cometary emission lines are clearly seen above the optimized atmospheric model spectrum (dashed curves). These emissions are numbered and indicated by arrows. The labeled emissions are identified as follows: 1. H_2O $\nu_3 - \nu_2$ (1_{11}–1_{10}), 2. CO (1–0) R1, 3. H_2O $\nu_1 - \nu_2$ (2_{21}–1_{10}), 4. CO (1–0) R0, 5. H_2O $\nu_3 - \nu_2$ (2_{12}–2_{11}), 6. CO (1–0) P1, 7. H_2O $\nu_3 - \nu_2$ (0_{00}–1_{01} and 3_{22}–3_{21}), 8. CO (1–0) P2 and H_2O $\nu_1 - \nu_2$ (4_{04}–3_{13}), 9. CN (1–0) P9, 10. H_2O $\nu_1 - \nu_2$ (1_{01}–2_{12}), 11. H_2O $\nu_1 - \nu_2$ (2_{12}–3_{03}) and CN P10.

3. Determination of the spatial distribution of H_2O

The high spectral and spatial resolution afforded by CSHELL provided an opportunity to measure the spatial distribution of H_2O and dust in the coma of Comet Ikeya–Zhang. The distribution of a species in the coma (along the slit, in our case) is termed its spatial profile (Fig. 3). The relatively close approach of Ikeya–Zhang to Earth during our observations (Table 1) allowed the distribution of H_2O in its coma to be sampled with high spatial resolution (each arc-second represented ~ 550 (340) km at the comet on UT 2002 March 21 (April 13)).

For spherically symmetric outflow at uniform velocity, the column density of a volatile (or dust) sublimed directly from the nucleus (with no additional distributed component) should fall off as ρ^{-1}, where ρ is the projected distance

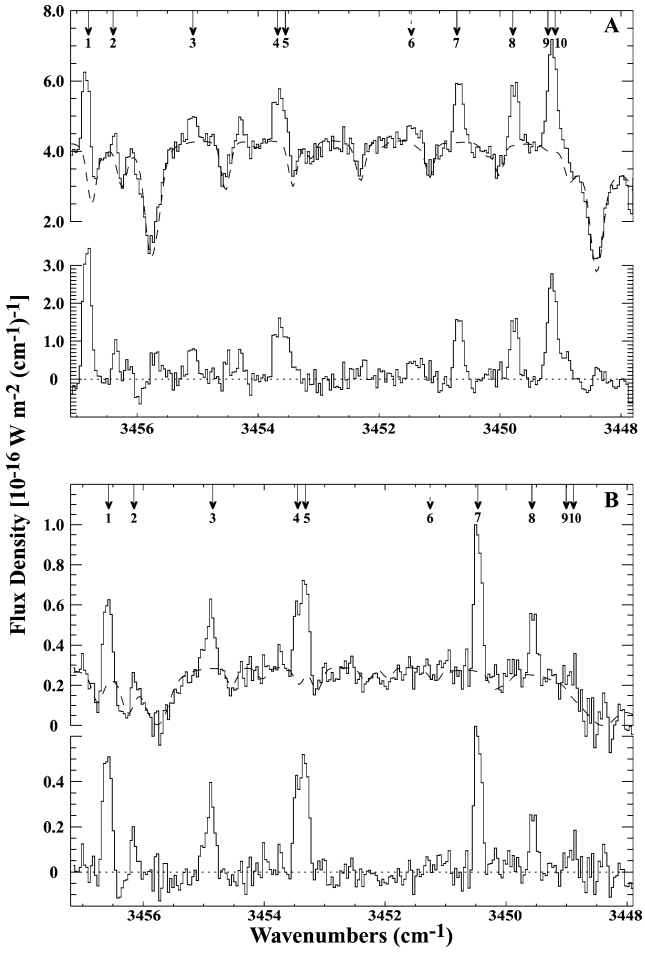

Fig. 2. Detection of 2.9-μm hot-band lines in Comet Ikeya–Zhang. (A) UT 2002 March 22, 00:31. (B) UT 2002 April 13, 18:45. Top: Flux-calibrated spectral extracts ($1'' \times 3''$) of Comet Ikeya–Zhang centered on the peak of the gas emission (solid curves). Cometary emissions are clearly seen above the optimized atmospheric model spectrum (dashed curves). These emissions are numbered and indicated by arrows. Bottom: Flux-calibrated residual spectral extracts ($1'' \times 3''$) of Comet Ikeya–Zhang centered on the peak of the gas emission (solid curves). These residuals are still convolved with the atmospheric transmittance function. The labeled emissions are identified as follows: 1. H_2O $\nu_1 + \nu_3 - \nu_1$ (4_{22}–5_{23}), 2. H_2O $2\nu_1 - \nu_1$ (3_{03}–4_{14}), 3. H_2O $\nu_1 + \nu_3 - \nu_3$ (2_{11}–2_{20}), 4. H_2O $2\nu_1 - \nu_1$ (1_{10}–2_{21}), 5. H_2O $\nu_1 + \nu_3 - \nu_1$ (2_{02}–3_{21}), 6. H_2O $\nu_1 + \nu_3 - \nu_3$ (4_{13}–4_{22}), 7. H_2O $2\nu_1 - \nu_3$ (1_{10}–1_{11}), 8. H_2O $\nu_1 + \nu_3 - \nu_1$ (5_{24}–6_{25}), 9. H_2O $\nu_1 + \nu_3 - \nu_1$ (6_{16}–7_{17}), 10. H_2O $\nu_1 + \nu_3 - \nu_1$ (6_{06}–7_{07}) and H_2O $\nu_1 + \nu_2 + \nu_3 - \nu_1 - \nu_2$ (5_{15}–6_{16}).

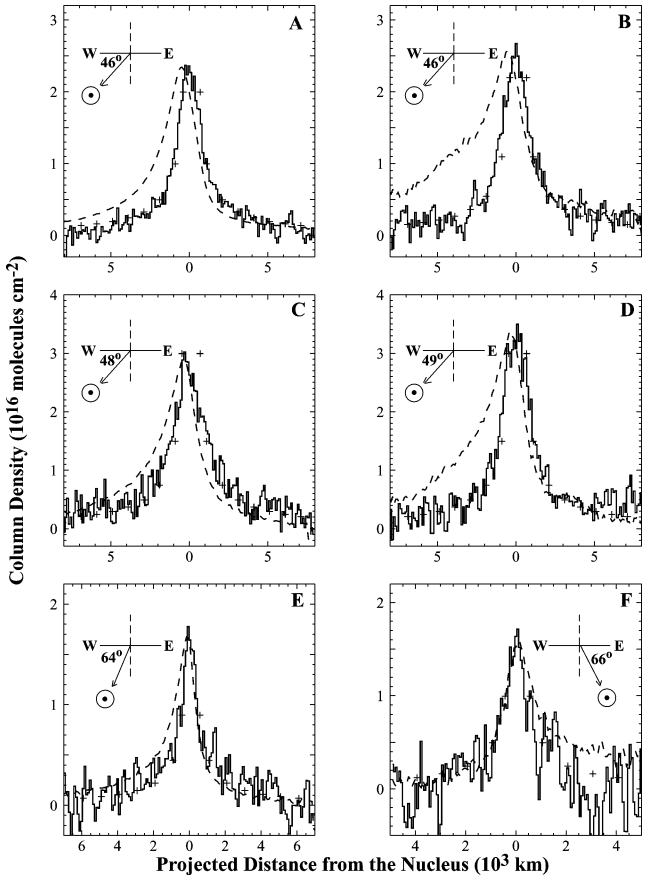

Fig. 3. Spatial profiles for H_2O (solid curves) and dust (dashed curves) in Comet Ikeya–Zhang. (A) UT 2002 March 21, 20:38. (B) UT 2002 March 22, 00:31. (C) UT 2002 March 22, 21:03. (D) UT 2002 March 23, 00:17. (E) UT 2002 March 27, 19:35. (F) UT 2002 April 10, 18:38. A ρ^{-1} distribution (+) is also shown on each panel. The H_2O profiles incorporate all lines from a particular grating setting. The slit was oriented east–west on all dates. The direction of the Sun with respect to the comet is indicated on each figure.

from the nucleus. This is valid as long as ρ is small compared to the photodissociation scale length of the species, as is the case for H_2O in Ikeya–Zhang on the dates observed. The spatial profile for a species released as a distributed source in the coma will be broader, falling off more slowly than ρ^{-1} (Dello Russo et al., 1998; DiSanti et al., 1999, 2001). However, outflow idiosyncrasies (e.g., jets), observing conditions, and optical depth effects can also affect profile shapes, causing deviations from a ρ^{-1} distribution even for purely native species (Dello Russo et al., 2000, 2001).

Following their release from the nucleus, collisions tend to isotropize the outflowing gas more rapidly than the dust (Xie and Mumma, 1996). So, in general, asymmetries in spatial profiles are more severe for dust than for parent volatiles. Spatial profiles for H_2O and simultaneously sampled dust are compared in Fig. 3 for different dates. The spatial profiles for water on all dates are very symmetric and closely follow a ρ^{-1} distribution beyond the seeing-affected region (within $\sim$ 500–1000 km from the peak of the water emission), while the simultaneously sampled dust shows significant asymmetries characterized by enhanced dust outflow in the sunward direction (Fig. 3). Comparison of the spatial profiles also shows that the peak of the dust emission was spatially offset from the peak of H_2O emission between UT March 21.9–23.0 (Figs. 3A–3D). Analysis of the spatial profiles indicates that most (if not all) water was released directly from the nucleus in Comet Ikeya–Zhang.

4. Development of H_2O hot-band fluorescence models

In hot-band fluorescence, direct absorption of solar photons excites molecules from the ground vibrational state

(000) to a higher vibrational state, followed by cascade into an intermediate vibrational state. In order to determine g-factors one needs to know:

(1) the initial population of rotational levels in the ground vibrational state;
(2) the pumping (and cascade) rates into individual rotational levels in the upper vibrational state of interest; and
(3) the rotational and vibrational branching ratios for the emitted lines.

Fluorescence models have been developed to determine g-factors as a function of temperature for ro-vibrational lines in eleven H_2O hot-bands (seven in the 2.9-μm region).

We illustrate the calculation of line-by-line g-factors, by considering the specific case of the $\nu_1 + \nu_3 - \nu_1$ (101–100) hot-band. We assume that the initial population distribution among rotational levels in the ground vibrational state is thermalized, i.e., is described by a Boltzmann distribution at a given temperature (the population of higher vibrational states is assumed to be negligible). The validity of this assumption is investigated in Appendix A. Pump rates from the ground to excited vibrational states were calculated from the solar flux at each wavelength using absorption coefficients taken from (Partridge and Schwenke, 1996; Schwenke and Partridge, 2000; Schermaul et al., 2001). Cascade from the 200 level was treated differently (see below).

An energy level diagram with some of the radiative transitions considered is shown in Fig. 4. The branching ratios for individual lines were obtained from band strengths and the vibrational Einstein A coefficients (see, e.g., Crovisier, 1984). Information on pump and cascade rates into the upper vibrational level, and vibrational branching ratios between the upper and lower vibrational levels are given in Table 2 for all bands of interest. The relative contributions of cascade and direct pumping for an individual upper level can vary greatly. For example, one level (100) is populated mainly by cascade, while the 101 vibrational level is primarily populated via direct pumping from the ground (000) state with only a minor contribution ($\sim 1\%$) by cascade from higher vibrational levels such as 111 (Fig. 4, Table 2).

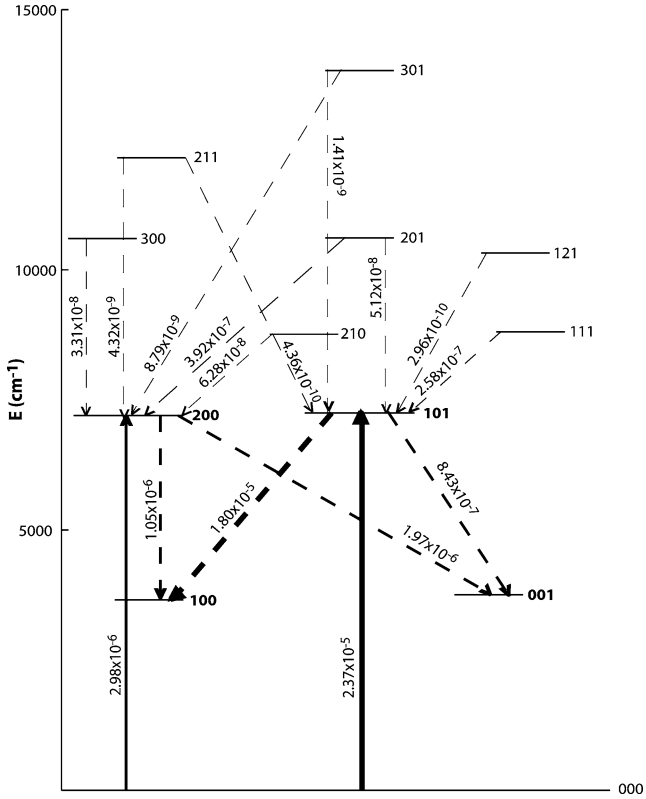

Fig. 4. Schematic showing pump and cascade rates (s^{-1}) for bands of interest near 2.9-μm (200–001, 200–100, 101–100, 101–001). The solid arrows indicate pump rates into the upper vibrational states, dashed arrows indicate cascade rates.

Our method for determining rotational branching ratios may present the largest source of uncertainty in developing water hot-band fluorescence models (see Appendix A). Laboratory measurements of absorption line strengths are not generally available for upward transitions from vibrationally excited states with energies higher than ν_2 (excitation energies exceed 4500 K for the next highest levels (020, 100, and 001) and it is difficult to populate them significantly in the laboratory). Therefore, we generally assume the vibrational modes are separable (one form of the Born approximation); in this case the transition probabilities

Table 2
g-factors for water hot-bands including vibrational branching ratios and pump and cascade rates into the upper vibrational level

V_{upper}	V_{lower}	Pump into V_{up} (s^{-1})[a]	Cascade into V_{up} (s^{-1})[b]	Total into V_{up} (s^{-1})[c]	BR_{vib}[d]	g_{band} (s^{-1})
ν_3	ν_2	2.67×10^{-4}	7.38×10^{-6}	2.74×10^{-4}	0.0275	7.52×10^{-6}
ν_1	ν_2	1.82×10^{-5}	2.31×10^{-5}	4.13×10^{-5}	0.223	9.20×10^{-6}
$\nu_1 + \nu_3$	ν_3	2.37×10^{-5}	3.11×10^{-7}	2.40×10^{-5}	0.0351	8.43×10^{-7}
$\nu_1 + \nu_3$	ν_1	2.37×10^{-5}	3.11×10^{-7}	2.40×10^{-5}	0.749	1.80×10^{-5}
$\nu_1 + \nu_2 + \nu_3$	$\nu_1 + \nu_2$	1.81×10^{-6}	2.05×10^{-8}	1.83×10^{-6}	0.553	1.01×10^{-6}
$2\nu_1$	ν_1	2.98×10^{-6}	5.01×10^{-7}	3.48×10^{-6}	0.301	1.05×10^{-6}
$2\nu_1$	ν_3	2.98×10^{-6}	5.01×10^{-7}	3.48×10^{-6}	0.567	1.97×10^{-6}

[a] Pump rate from the ground vibrational level (000) into V_{upper}.
[b] Cascade rate from higher vibrational levels into V_{upper}.
[c] Total contributions from pump and cascade into V_{upper}.
[d] Vibrational branching ratio from V_{upper} to V_{lower}.

within a hot-band (e.g., 100 → 101) are the same as those for the corresponding fundamental band (e.g., 000 → 001). The absorption line strengths for fundamental bands are tabulated in several places (e.g., Rothman et al. (1992) and radiative transition probabilities (Einstein A's) are calculated from them in the usual way (e.g., Crovisier, 1984; Weaver and Mumma, 1984). The sum of direct and cascade pumping into a given upper level is estimated in this way. The pump rates are multiplied by branching ratios into given lower levels, yielding line-by-line temperature-dependent fluorescence g-factors (for more details on the methodology see the appendix in Dello Russo et al., 2000).

In developing these models, we initially took the vibrational Einstein A coefficients for crossed transitions (also known as difference bands for which there is a transfer of energy between different modes of vibration) to be negligible (Crovisier, 1984). This is a valid assumption in general, however, ro-vibrational lines from the crossed 200 → 001 transition have been seen in laboratory spectra of hot H_2O and in sunspot spectra (cf. Zobov et al., 2000). Positions for the strongest 200 → 001 ro-vibrational lines at temperatures relevant to comets were calculated using ro-vibrational energy level data (Tennyson et al., 2001). This calculation was consistent with the presence of a strong line from the 200 → 001 hot-band in Ikeya–Zhang. This identification was confirmed when multiple strong lines from the 200 → 001 hot-band were present in the spectra of other comets within our database (Dello Russo et al., in preparation).

The 200 level can be pumped directly (000 → 200) or by cascade (000 → 201 → 200). The contribution due to cascade was obtained by evaluating the transfer of intensities from the corresponding ν_3 fundamental band (Fig. 4, Table 2). Direct pump rates for 000 → 200 and vibrational branching ratios for the 200 → 100 and 200 → 001 hot-bands were determined (Fig. 4, Table 2). Einstein A coefficients for 200 → 100 and 200 → 001 transitions were computed using first principles variational nuclear motion calculations. Energy levels and wavefunctions were calculated using program DVR3D (Tennyson et al., 2003) and the recent, spectroscopically-determined, potential energy surface of Shirin et al. (2003). Einstein A coefficients were then calculated using these wavefunctions and the ab initio dipole surface of Lynas-Gray et al. (in preparation). These calculations used very highly converged wavefunctions as they are part of a much more extensive study designed for modeling the spectrum of hot water. The full calculations will be reported elsewhere.

5. Determination of H_2O rotational temperatures

Knowledge of the rotational temperature is needed to determine total production rates from individual line intensities. Conversely, the temperature dependence of g-factors for individual ro-vibrational lines ($g_{\rm line}$) is needed to obtain an effective rotational temperature from the measured line intensities (Table 3). We first assume that a single rotational temperature characterizes all rotational levels in the ground vibrational state. We then estimate the rotational temperature ($T_{\rm rot}$) in the ground vibrational state by comparing the transmittance-corrected H_2O line fluxes ($F_{\rm line}$) with their calculated g-factors, using all measured lines within a grating setting. These g-factors vary with rotational temperature. The measured line fluxes reflect the populations of the rotational levels in the upper vibrational state (that in turn reflect the temperature-dependent distribution in the ground state). In general, a single upper state rotational level is pumped from several different levels in the ground vibrational state. The average energy of these lower state levels (weighted by their relative contributions to the upper state population) approximates the energy of the upper state ($E_u - E_u(0_{00})$) that they are populating. At the correct rotational temperature, $F_{\rm line}/g_{\rm line}$ should be independent of ($E_u - E_u(0_{00})$). For this reason, the retrieved rotational temperature is most accurate when a wide range of rotational energy states are sampled.

Table 3
Log of detected water lines

H_2O band	H_2O line	ν rest (cm^{-1})	$E_u - E_u(0_{00})$ (cm^{-1})	$g_{100\ K}$[a] 10^{-8} s^{-1}	$g_{120\ K}$[a] 10^{-8} s^{-1}	$g_{150\ K}$[a] 10^{-8} s^{-1}
100–010	2_{12}–3_{03}	2003.00	79.50	22.1	20.6	18.4
100–010	1_{01}–2_{12}	2003.39	23.79	41.7	36.0	29.5
001–010	3_{22}–3_{21}	2137.33	206.30	6.84	8.06	9.12
001–010	0_{00}–1_{01}	2137.37	0.00	48.7	39.5	30.2
001–010	2_{12}–2_{11}	2139.92	79.50	5.00	4.59	4.02
100–010	2_{21}–1_{10}	2148.19	134.90	14.2	14.5	14.4
001–010	1_{11}–1_{10}	2151.19	37.14	45.4	39.8	33.0
111–110	5_{15}–6_{16}	3448.72	326.63	0.94	1.28	1.68
101–100	6_{06}–7_{07}	3448.74	446.70	4.79	8.26	13.7
101–100	6_{16}–7_{17}	3448.83	447.25	1.58	2.73	4.55
101–100	5_{24}–6_{25}	3449.38	416.21	4.74	7.78	12.3
200–001	1_{10}–1_{11}	3450.29	42.37	10.2	8.87	7.35
101–100	2_{02}–3_{21}	3453.15	70.09	6.93	6.07	5.08
200–100	1_{10}–2_{21}	3453.30	42.37	7.27	6.31	5.23
101–001	2_{11}–2_{20}	3454.69	95.18	4.60	4.16	3.59
200–100	3_{03}–4_{14}	3455.98	136.76	4.03	4.14	4.07
101–100	4_{22}–5_{23}	3456.45	315.78	7.31	9.67	12.4

[a] Line g-factors derived at the indicated rotational temperature. The ortho-to-para ratio (OPR) is assumed to be 3.0.

It is difficult to determine $T_{\rm rot}$ from hot-band lines near 4.7 and 5.0-μm alone, since only two strong hot-bands fall in this region and they provide only a limited number of lines within a single grating setting (Fig. 1). Thus, several grating settings are needed to sample a sufficient number of lines, introducing errors associated with relative flux calibration among different grating settings. In addition, many of the strong lines have g-factors that vary similarly with temperature (the transitions are pumped from states with similar lower state rotational energies), while other lines better suited for a rotational temperature analysis are often too weak, or are accidentally coincident with telluric absorption features. As a result, rotational temperatures are more difficult to constrain in this spectral region, causing larger uncertainties in the retrieved values.

To avoid this problem we target water hot-band lines near 2.9-μm. This region contains several strong water hot-

bands, enabling lines with a wide range of upper state rotational energies to be sampled within a single grating setting (Fig. 2, Table 3). This allows a more accurate determination of rotational temperature. To illustrate this point, we compared the observed residuals of Comet Ikeya–Zhang (showing molecular emissions) on two dates with our synthetic H_2O models multiplied by the atmospheric transmittance at each Doppler-shifted line frequency and convolved to the approximate resolution of the cometary spectra (Fig. 5).

Also, as mentioned above, the ratio of line fluxes to line g-factors ($F_{\rm line}/g_{\rm line}$) should remain constant over a range of upper state rotational energies at the correct rotational temperature, if a single rotational temperature applies to the ground vibrational level. It is convenient to show the ratio of $F_{\rm line}/g_{\rm line}$ as a function of upper state rotational energy ($E_u - E_u(0_{00})$, where $E_u(0_{00})$ represents the lowest lying rotational level in the upper state) (Fig. 6). In a strict sense,

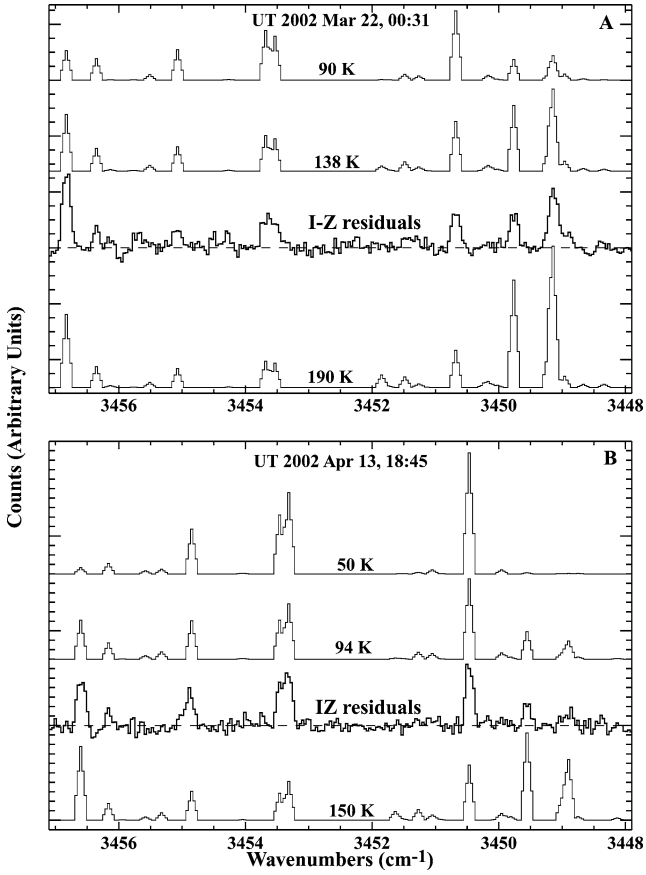

Fig. 5. Comparison of Ikeya–Zhang spectral extracts to model predictions for H_2O at various rotational temperatures. Residual spectral extracts (still convolved with the atmospheric transmittance function) are compared to synthetic H_2O spectra based on fluorescence models developed for seven hot-bands. The comet residuals are $1'' \times 3''$ extracts centered on the peak of the H_2O emission. The synthetic H_2O spectra are multiplied by the atmospheric transmittance at each Doppler-shifted line frequency and convolved to the approximate resolution of the cometary spectra. (A) Spectra from top to bottom: 1. Synthetic H_2O spectrum at 90 K. 2. Synthetic H_2O spectrum at 138 K (derived rotational temperature in Ikeya–Zhang on this date). 3. Residual Ikeya–Zhang spectrum on UT 2002 March 22, 00:31. 4. Synthetic H_2O spectrum at 190 K. (B) Spectra from top to bottom: 1. Synthetic H_2O spectrum at 50 K. 2. Synthetic H_2O spectrum at 94 K (derived rotational temperature in Ikeya–Zhang on this date). 3. Residual Ikeya–Zhang spectrum on UT 2002 April 13, 18:45. 4. Synthetic H_2O spectrum at 150 K.

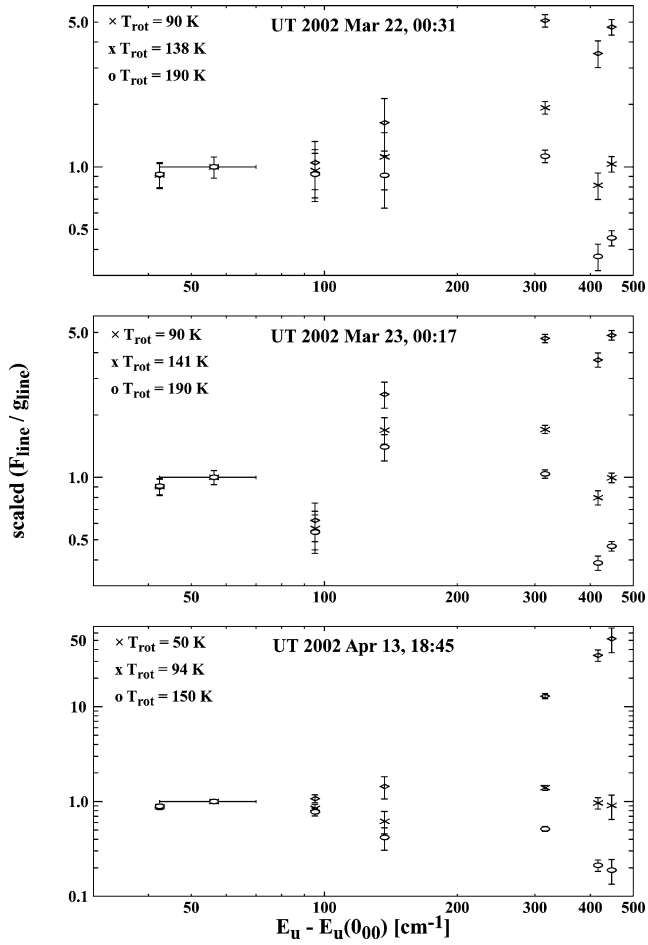

Fig. 6. Rotational temperature analysis for H_2O in Comet Ikeya–Zhang for the three dates that a rotational temperature was measured using lines at 2.9-μm. The scaled ratio of the transmittance-corrected line flux ($F_{\rm line}$) to the line g-factor ($g_{\rm line}$) is shown vs. upper state rotational energy ($E_u - E_u(0_{00})$). The lines and fluxes used in the analysis are listed in Table 4 on the appropriate UT date and time. The upper state rotational energies and g-factors as a function of temperature for the 2.9-μm lines used in the analysis are listed in Table 3. Blended lines display horizontal error bars representing the range in upper state energies sampled. One emission feature is the result of a blend of 3 lines (see Table 3, and lines 9 and 10 in Fig. 2), however horizontal error bars do not include the upper state rotational energy of the H_2O $\nu_1 + \nu_2 + \nu_3 - \nu_1 - \nu_2$ (5_{15}–6_{16}) line ($E_u = 326.63$ cm^{-1}) since it contributes only $\sim$ 8–10% to the total flux of the blended feature (see Table 3). Vertical error bars represent the estimated errors in $F_{\rm line}$ within a $1'' \times 3''$ aperture centered on the peak of the H_2O emission. The ratio $F_{\rm line}/g_{\rm line}$ should be constant over a range of upper state rotational energies at the correct rotational temperature (x's). For a model rotational temperature that is too low, the ratio $F_{\rm line}/g_{\rm line}$ should increase with increasing upper state energy (diamonds). For a model rotational temperature that is too high, the ratio $F_{\rm line}/g_{\rm line}$ should decrease with increasing upper state energy (circles). The ratio $F_{\rm line}/g_{\rm line}$ is multiplied by a constant so that the scaled $F_{\rm line}/g_{\rm line} = 1$ for the blended emission $2\nu_1 - \nu_1$ (1_{10}–2_{21}), $\nu_1 + \nu_3 - \nu_1$ (2_{02}–3_{21}). We note that the 101–100 4_{22}–5_{23} line ($E_u - E_u(0_{00}) = 315.78$ cm^{-1}) was not used in the determination of rotational temperatures since it is suspected to be blended with an unknown emission feature (see text).

one should show the ratio of $F_{\rm line}/g_{\rm line}$ as a function of the weighted average of rotational energies in the lower state, however this is less straightforward and makes no significant difference in the retrieved rotational temperatures. Displaying the data as in Fig. 6 permits visual identification of systematic differences while also enhancing evaluation of individual spectral lines. Upper state rotational energies for relevant lines are given in Table 3.

Using hot-band lines at 2.9-μm we were able to derive H_2O rotational temperatures on three dates. All lines at 2.9-μm were used in this analysis except the 101–100 4_{22}–5_{23} line at rest frequency 3456.45 cm^{-1} ($E_u - E_u(0_{00}) = 315.78$ cm^{-1}) because it is suspected to be blended with an unknown emission feature (see Discussion and Appendix A). The derived rotational temperatures are 138^{+6}_{-5}, 141^{+10}_{-9}, and 94 ± 3 K for UT March 22.0, March 23.0, and April 13.8, respectively (Table 4, Figs. 5, 6). These rotational temperatures (with 1σ errors) were derived from lines within a single grating setting, and $F_{\rm line}$ was determined within a $1'' \times 3''$ aperture centered on the peak of the water emission (Table 4). We note that the derived rotational temperature should be considered an average over this aperture, since it is possible that the temperature was non-uniform in this region (although within the sensitivity of our

Table 4
Water hot-band lines detected in Comet Ikeya–Zhang

H_2O band	H_2O line	ν rest (cm^{-1})	UT date 2002	F_1[a]	F_2[b]	$T_{\rm rot}$[c]	Q_{H_2O}[d]
100–010	2_{21}–1_{10}	2148.19	3/21 20:38	280	158	138[f]	6.74 ± 0.94
001–010	1_{11}–1_{10}	2151.19		725	408		7.14 ± 0.39
101–100	6_{06}–7_{07}	3448.72	3/22 00:31				
111–110	5_{15}–6_{16}	3448.74		591	300	138^{+6}_{-5}	8.12 ± 0.69
101–100	6_{16}–7_{17}	3448.83					
101–100	5_{24}–6_{25}	3449.38		290	153		6.41 ± 0.94
200–001	1_{10}–1_{11}	3450.29		245	167		7.22 ± 0.99
101–100	2_{02}–3_{21}	3453.15		374	187		7.88 ± 0.92
200–100	1_{10}–2_{21}	3453.30					
101–001	2_{11}–2_{20}	3454.69		124	107		7.58 ± 1.98
200–100	3_{03}–4_{14}	3455.98		156	118		8.8 ± 2.7
101–100	4_{22}–5_{23}	3456.45		745	514		15.2 ± 1.1[g]
001–010	3_{22}–3_{21}	2137.33	3/22 00:40	720	488	138[f]	7.05 ± 0.41
001–010	0_{00}–1_{01}	2137.37					
001–010	2_{12}–2_{11}	2139.92		107	51		7.4 ± 2.0
100–010	2_{21}–1_{10}	2148.19	3/22 20:34	215	274	138[f]	11.4 ± 2.0
001–010	1_{11}–1_{10}	2151.19		613	438		7.49 ± 0.58
100–010	2_{12}–3_{03}	2003.00	3/22 21:03	[e]	[e]	138[f]	[e]
100–010	1_{01}–2_{12}	2003.39		796	462		9.39 ± 0.70
101–100	6_{06}–7_{07}	3448.72	3/23 00:17				
111–110	5_{15}–6_{16}	3448.74		876	528	141^{+10}_{-9}	10.98 ± 0.58
101–100	6_{16}–7_{17}	3448.83					
101–100	5_{24}–6_{25}	3449.38		438	271		8.87 ± 0.69
200–001	1_{10}–1_{11}	3450.29		349	244		10.02 ± 0.90
101–100	2_{02}–3_{21}	3453.15		541	280		11.08 ± 0.87
200–100	1_{10}–2_{21}	3453.30					
101–001	2_{11}–2_{20}	3454.69		106	63		6.27 ± 1.32
200–100	3_{03}–4_{14}	3455.98		347	201		18.7 ± 2.7
101–100	4_{22}–5_{23}	3456.45		994	530		18.9 ± 0.9[g]
001–010	1_{11}–1_{10}	2151.19	3/27 19:35	762	465	120[f]	5.97 ± 0.53
001–010	1_{11}–1_{10}	2151.19	4/10 18:29	212	113	100[f]	1.96 ± 0.14
001–010	1_{11}–1_{10}	2151.19	4/10 18:38	264	171	100[f]	2.20 ± 0.25
001–010	3_{22}–3_{21}	2137.33	4/10 19:10	287	134	100[f]	1.89 ± 0.16
001–010	0_{00}–1_{01}	2137.37					
001–010	1_{11}–1_{10}	2151.19	4/11 19:50	272	151	100[f]	2.56 ± 0.20
001–010	1_{11}–1_{10}	2151.19	4/11 21:32	240	145	100[f]	2.62 ± 0.37
001–010	1_{11}–1_{10}	2151.19	4/11 21:52	235	165	100[f]	2.82 ± 0.39
001–010	1_{11}–1_{10}	2151.19	4/12 17:48	495	200	100[f]	3.61 ± 0.23
001–010	3_{22}–3_{21}	2137.33	4/12 21:25	342	156	100[f]	2.36 ± 0.26
001–010	0_{00}–1_{01}	2137.37					
001–010	1_{11}–1_{10}	2151.19	4/12 21:48	303	149	100[f]	2.78 ± 0.25
001–010	1_{11}–1_{10}	2151.19	4/13 17:33	224	126	94[f]	2.11 ± 0.19
101–100	6_{06}–7_{07}	3448.72	4/13 18:45				
111–110	5_{15}–6_{16}	3448.74		62	17	94 ± 3	1.76 ± 0.51
101–100	6_{16}–7_{17}	3448.83					

(*continued on next page*)

Table 4 (*continued*)

H_2O band	H_2O line	ν rest (cm^{-1})	UT date 2002	F_1[a]	F_2[b]	T_{rot}[c]	Q_{H_2O}[d]
101–100	5_{24}–6_{25}	3449.38		43	19		1.84 ± 0.25
200–001	1_{10}–1_{11}	3450.29		108	38		1.68 ± 0.09
101–100	2_{02}–3_{21}	3453.15		170	61		1.89 ± 0.09
200–100	1_{10}–2_{21}	3453.30					
101–001	2_{11}–2_{20}	3454.69		46	17		1.63 ± 0.16
200–100	3_{03}–4_{14}	3455.98		28	12		1.17 ± 0.31
101–100	4_{22}–5_{23}	3456.45		105	32		2.65 ± 0.16[g]
001–010	3_{22}–3_{21}	2137.33	4/13 20:10	255	90	94[f]	1.33 ± 0.19
001–010	0_{00}–1_{01}	2137.37					
001–010	2_{12}–2_{11}	2139.92		43	18		2.94 ± 0.98

[a] F_1 is the total transmittance-corrected line flux (10^{-19} W m^{-2}) in an aperture $1'' \times 3''$ (15 spatial × 5 spectral pixels) in size and centered on the peak of the water emission.

[b] F_2 is the total transmittance-corrected line flux (10^{-19} W m^{-2}) in an aperture $1'' \times 7''$ ($1'' \times 4''$) in size over the range 1.5″–8.5″ (1.5″–5.5″) off the peak of the water emission, averaged east and west for water lines in settings that were nodded off-(on-) chip (see Table 1). Water production rates were determined over the same range for grating settings near 5-μm (see text).

[c] Rotational temperatures (K) were derived on UT March 22.0, March 23.0, and April 13.8 from the 2.9-μm water lines in an aperture $1'' \times 3''$ in size and centered on the peak of the water emission. Rotational temperatures derived from extracts off the peak of the water emission agree within the errors. Errors in T_{rot} are 1σ.

[d] Q_{H_2O} is the line-by-line water production rate (10^{29} molecules s^{-1}). Calibration errors are not included.

[e] No line flux or production rate was determined for this line since it is blended with a CN emission.

[f] Assumed rotational temperature. The error in T_{rot} is assumed to be ±10 K.

[g] Not included in the determination of T_{rot} or production rates in Table 5 (see text).

measurements there is no evidence of this). The errors on the derived T_{rot} reflect the variance of the point-by-point F_{line}/g_{line} from the mean (which is larger than that derived from individual error bars in Fig. 6). On other dates, reasonable rotational temperatures were adopted (Table 4; the error on adopted rotational temperatures is assumed to be ±10 K).

The results imply that the rotational temperature decreased by about 40–50 K between UT March 22.0 ($R_h = 0.51$) and UT April 13.8 ($R_h = 0.78$ AU) (Figs. 5, 6). This is not unexpected, since the comet was receding from the Sun during this period of time. A decrease in T_{rot} with heliocentric distance has been seen for several molecules in other comets, although the R_h-dependence can vary (cf. Biver et al., 1999, 2002; Dello Russo et al., 2000; DiSanti et al., 2001). The formal relationship derived from our results for Ikeya–Zhang is $T_{rot} = (74 \pm 4)[R_h^{(-0.93\pm0.11)}]$ K.

6. Determination of H_2O production rates

The high spectral and spatial resolution afforded by CSHELL allows production rates to be determined from intensities of strong molecular emissions measured at different positions along the slit. The methodology for determining production rates and generating "Q-curves" is discussed in detail elsewhere (see Dello Russo et al., 1998, 2000, 2001, 2002a; Magee-Sauer et al., 1999, 2002a; DiSanti et al., 2001, for detailed discussion and examples). A brief discussion for the case of Comet Ikeya–Zhang follows.

Assuming uniform spherical outflow, production rates can be determined at different spatial positions along the slit. When a $1'' \times 1''$ box is stepped at $1''$ intervals along the length of the slit, the sequence of "spherical" production rates constitutes a Q-curve. "Symmetric" production rates were determined by taking the average of spherical production rates at corresponding distances east and west of the nucleus. Production rates derived from nucleus-centered extracts are always lower than those derived at positions offset from the nucleus due to factors including seeing, drift, and telescope de-focusing (typically the flux measured in a $1'' \times 1''$ box centered on the nucleus is less than that expected in the absence of these effects by about a factor of 2–5). The flux is underestimated only for regions within the PSF and the symmetric production rates reach a constant (terminal) value between (typically) 1″–2″ from the nucleus. For H_2O lines in the 4.7 and 5.0-μm region the 'global' production rates determined for each individual line were taken from a weighted average of symmetric production rates over the terminal region (Table 4). Global production rates were determined between 1.5″–8.5″ from the center of the peak of the gas emission for observations nodded off-chip, and between 1.5″–5.5″ from the gas emission peak for on-chip nods (nod information on each grating setting is given in Table 1).

For water lines near 2.9-μm, a slightly different technique was used. Global production rates were determined within a $1'' \times 3''$ extract centered on the nucleus. Since the "raw" nucleus-centered production rate underestimates the true production rate, a correction factor based on the ratio of terminal to nucleus-centered production rates was applied. The correction factor was determined from the ratio of terminal to nucleus-centered production rates derived from the summed H_2O Q-curve (based on the spatial profile representing the sum of all water lines within the grating setting, e.g., Figs. 3B, 3D). The correction factor was applied to the derived production rate for each individual line. This is assumed to be valid since all lines within a single grating

setting will be equally affected by seeing, drift, and telescope de-focusing. In grating settings with many lines, this technique has the advantage of sampling the region with the highest signal-to-noise ratio. Line-by-line global production rates for 2.9-μm H_2O lines are given in Table 4.

We adopt a model in which all H_2O is produced at the nucleus and is released into the coma with spherical symmetry and with uniform velocity. The production rate (Q, molecules s^{-1}) is calculated as follows:

$$Q = \frac{4\pi \Delta^2 F_i}{g_i \tau (hc\nu) f(x)}. \quad (1)$$

The geocentric distance Δ is in meters, $hc\nu$ is the energy (J) of a photon with wavenumber ν (cm^{-1}), and $f(x)$ is the fraction of molecules expected in the sampled region (x being the fraction of a photodissociation scale length subtended by the aperture radius; see appendix of Hoban et al., 1991). The photodissociation lifetime τ (s) and line g-factor g_i (photons s^{-1} molecule^{-1}) are both calculated for $R_h = 1$ AU. The flux (W m^{-2}) from the ith line incident atop the terrestrial atmosphere is denoted F_i.

For an aperture diameter much smaller than the destruction scale length, $f(x) \propto (\tau v_{\rm gas})^{-1}$; inspection of Eq. (1) shows that our derived Q's are not sensitive to the lifetime assumed but they are sensitive to the outflow velocity. We assumed the standard photodissociation lifetime for quiet Sun conditions ($\tau_{H_2O} = 7.7 \times 10^4$ s; Crovisier, 1989), and a gas outflow velocity ($v_{\rm gas} = 0.8 R_h^{-0.5}$ km s^{-1}). This is approximately the gas outflow velocity determined for C/1996 B2 Hyakutake (Biver et al., 1999), a comet similar to Ikeya–Zhang in total gas production rate.

Production rates were determined for each of the nineteen grating settings that contained H_2O lines and for each of the seven observing periods (Table 5). These production rates represent a weighted average of Q's obtained from individual line measurements listed in Table 4. An ortho-to-para ratio (OPR) could not be determined since no strong unblended para lines were sampled, so OPR = 3.0 was assumed (OPR = 3.0 indicates a nuclear spin temperature ($T_{\rm spin}$) $\geqslant$ 50 K). An OPR of less than 3.0 would increase our derived production rates (for OPR = 2.2 ($T_{\rm spin} \sim 25$ K), derived production rates would increase by $\sim$ 9% on all dates). The global H_2O production rates derived for each individual observing period (Table 5) were generally based on multiple ro-vibrational lines from several different hot-bands (Table 4). The self-consistency of our data processing algorithms and fluorescence efficiency models for H_2O is demonstrated by the general agreement among production rates derived from lines in different hot-bands (Table 4).

Errors were evaluated line-by-line for each date. The uncertainties in global production rates for lines in the 4.7 and 5.0-μm region were determined by comparing the standard deviation from the mean of symmetric production rates (over the terminal region) with the error due to photon noise, and taking the higher value. For data having high (stochastic) signal-to-noise, the error was usually dominated by the standard deviation of the symmetric production rates over the terminal region. This includes factors such as deviations in the synthetic atmospheric model fit, instrumental effects, possible spatial variations in rotational temperature and outflow velocity, and other factors that cause deviations from our idealized gas outflow model. For the 2.9-μm lines, the uncertainties in global production rates were determined by the error due to photon noise in a $1'' \times 3''$ extract centered on the nucleus. In addition it is estimated that $\sim$ 10% error exists in the flux calibration of each grating setting. This error in flux calibration is applied to Q's obtained within a grating setting as listed in Table 5. It is not applied to individual lines in Table 4.

Table 5
Water production rates in Comet Ikeya–Zhang by grating setting and date

UT date 2002	UT time	Q (10^{29} molecules s^{-1})[a]	Q (10^{29} molecules s^{-1})[b]
21 Mar	20:38	7.08 ± 0.79	
22 Mar	00:31	7.57 ± 0.81	7.23 ± 0.46
22 Mar	00:40	7.06 ± 0.81	
22 Mar	20:34	7.79 ± 1.31	
22 Mar	21:03	9.39 ± 1.17	9.14 ± 0.72
23 Mar	00:17	10.13 ± 1.28	
27 Mar	19:35	5.97 ± 0.80	5.97 ± 0.80
10 Apr	18:29	1.96 ± 0.24	
10 Apr	18:38	2.20 ± 0.33	1.99 ± 0.15
10 Apr	19:10	1.89 ± 0.25	
11 Apr	19:50	2.56 ± 0.32	
11 Apr	21:32	2.62 ± 0.45	2.63 ± 0.23
11 Apr	21:52	2.82 ± 0.48	
12 Apr	17:48	3.61 ± 0.43	
12 Apr	21:25	2.36 ± 0.35	2.83 ± 0.35
12 Apr	21:48	2.78 ± 0.37	
13 Apr	17:33	2.11 ± 0.29	
13 Apr	18:45	1.75 ± 0.19	1.77 ± 0.17
13 Apr	20:10	1.39 ± 0.34	

[a] Water production rates determined from a weighted average of all lines sampled within a grating setting. Calibration errors are included.

[b] Water production rates determined from a weighted average of values obtained from each grating setting sampled during a single observing period.

Our H_2O production rates are shown vs. heliocentric distance in Fig. 7 (each point in Fig. 7 is taken from column 3 in Table 5 and represents a separate grating setting). A least squares fit to values obtained in our nineteen grating settings yielded $Q_{H_2O} = (9.2 \pm 1.1) \times 10^{28} [R_h^{(-3.21 \pm 0.26)}]$ molecules s^{-1} between $R_h = 0.51$–0.78 AU post-perihelion.

7. Discussion

Production rates derived from different hot-bands are in general agreement, but line-by-line values show significant scatter (especially in the 2.9-μm region; Table 4). Some values appear to be systematically high or low on specific dates (e.g., 101–100 4_{22}–5_{23} line, see below). The likely cause of this scatter is uncertainty in the branching ratios for individual hot-band transitions and/or blending with unknown

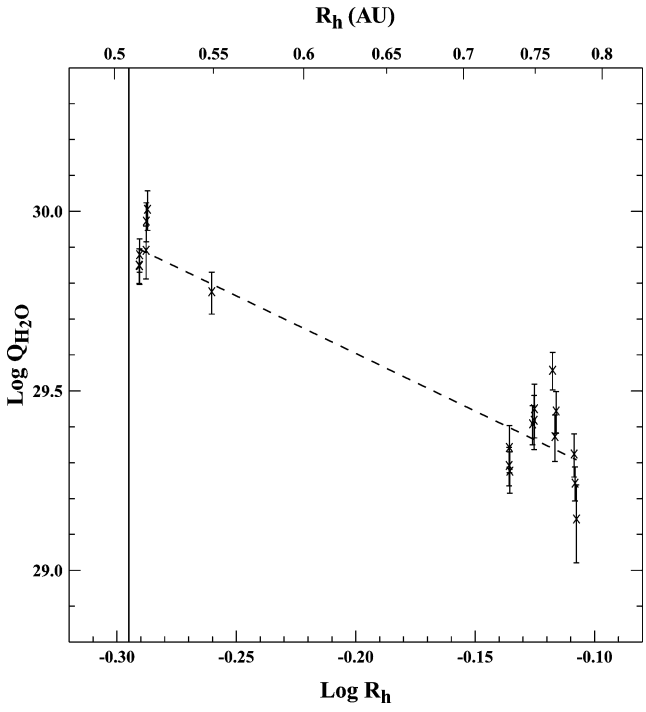

Fig. 7. Evolution of the water production rate in Comet Ikeya–Zhang with heliocentric distance R_h. The solid vertical line represents the heliocentric distance at perihelion. The dashed line is the post-perihelion heliocentric dependence, $Q_{H_2O} = (9.2 \pm 1.1) \times 10^{28} [R_h^{(-3.21 \pm 0.26)}]$ molecules s^{-1}, derived from a least squares fit to our measured values (x's). These values (19 measurements) are taken from the third column in Table 5.

emissions; several other potential factors were considered but were found to be unimportant (see Appendix A). We now consider the possible impact of deviant data points on our retrieved rotational temperatures and production rates.

Rotational temperatures were derived on three dates; the values listed in Table 4 include all lines detected at 2.9-μm except the 101–100 4_{22}–5_{23} line (the analysis is illustrated in Figs. 5 and 6). The 101–100 4_{22}–5_{23} line displayed an unexpectedly high flux and correspondingly high production rate on all three dates (for this line $E_u - E_u(0_{00}) = 315.78$ in Fig. 6 and Table 4)—its production rate differs from the mean production rate derived from other lines by an amount much larger than its confidence limits. Excluding this line from the analysis decreases the 1σ error bars of the mean rotational temperature, but makes little difference in the mean value itself (e.g., the temperature retrieved when including this line on UT March 22.0, ($T_{rot} = 141^{+10}_{-9}$ K) is revised to $T_{rot} = 138^{+6}_{-5}$ K upon its removal). This agreement demonstrates that sampling lines with a range of upper state rotational energies largely compensates for the scatter among the data, enhancing extraction of well-constrained rotational temperatures.

Removal of the 101–100 4_{22}–5_{23} line from the analysis affects the Q derived for that grating setting. For example, on UT 00:31 March 22, inclusion of that point results in a derived production rate for that grating setting of $(8.52 \pm 1.36) \times 10^{29}$ molecules s^{-1} compared to $(7.57 \pm 0.81) \times 10^{29}$ molecules s^{-1} when it is excluded (Table 5, column 3). This line was excluded from the analysis of H_2O production rates by grating setting for all dates (Table 5, column 3). All other lines listed in Table 4 were included when retrieving production rates by grating setting and date (Table 5).

8. Summary

Direct detection of water from ground-based observatories has historically been problematic due to severe atmospheric extinction and low spectral resolution. To avoid this problem, we target cometary H_2O lines in non-resonance (hot-band) fluorescence, using high-resolution spectrometers such as CSHELL at the IRTF. We have traditionally targeted water hot-band lines near 2, 4.7, and 5-μm. However, determining accurate rotational temperatures from these emissions is difficult due to a relative paucity of strong lines that span a sufficient range of lower state rotational energies. Several different grating settings must be sampled to constrain a rotational temperature in these spectral regions, introducing additional calibration uncertainties.

We address this problem by targeting H_2O hot-band lines near 2.9-μm. Several strong hot-bands are present in this region, enabling the determination of rotational temperature from lines detected within a single grating setting. Lines with a range of lower state rotational energies are sampled, permitting the determination of accurate rotational temperatures (Figs. 5, 6). We derived H_2O rotational temperatures in Comet Ikeya–Zhang with this approach, finding T_{rot} to be 138^{+6}_{-5}, 141^{+10}_{-9}, and 94 ± 3 K for UT March 22.0, March 23.0, and April 13.8, respectively.

We also measured the spatial distribution of H_2O and dust in the coma of Comet Ikeya–Zhang. The spatial profiles for water on all dates are very symmetric and closely follow a ρ^{-1} distribution beyond the seeing-affected region, while the simultaneously sampled dust shows significant asymmetries and enhanced production in the sunward-facing hemisphere (Fig. 3). Analysis of spatial profiles indicates that most (if not all) water was released directly from the nucleus in Comet Ikeya–Zhang.

We derived H_2O production rates from lines in at least six different hot-bands obtained in nineteen grating settings over seven observing periods between UT 2002 March 21.9–April 13.9 (Tables 1, 4, 5). The self-consistency of our data processing algorithms and fluorescence efficiency models for H_2O is demonstrated by the general agreement among production rates derived from lines in different hot-bands (Table 4). A least-squares fit to values obtained in these grating settings revealed the water production rate as a function of heliocentric distance between $R_h = 0.51$–0.78 AU post-perihelion to be: $Q_{H_2O} = (9.2 \pm 1.1) \times 10^{28} [R_h^{(-3.21 \pm 0.26)}]$ molecules s^{-1} (Fig. 7).

Our H_2O production rates can be compared to production rates inferred from the detection of its photodissociation products. H_2O production rates also provide a basis for

comparison with other volatile species observed in Ikeya–Zhang (cf. Dello Russo et al., 2002b; DiSanti et al., 2002; Gibb et al., 2002; Magee-Sauer et al., 2002b). Comparison of relative abundances in comets to abundances in interstellar and nebular material may help to constrain the origin of pre-cometary ices and their processing histories.

Acknowledgments

This work was supported by the NASA OSS Planetary Atmospheres Program under NAG5-10795 to N. Dello Russo and the Planetary Astronomy Program under RTOP 693-344-32-30-07 to M.J. Mumma. We thank A. Tokunaga and the IRTF staff for accommodating our request for TOO time while the comet was at its brightest and available only during daytime. We also thank D. Griep and L. Bergknut for their expertise allowing us to successfully obtain these data during difficult observing conditions. The NASA IRTF is operated by the University of Hawaii under Cooperative Agreement number NCC 5-538 with the NASA OSS Planetary Astronomy Program. The authors recognize and acknowledge the very significant cultural role and reverence that the summit of Mauna Kea has always had within the indigenous Hawaiian community. We are most fortunate to have the opportunity to conduct observations from this mountain.

Appendix A

Production rates derived from different hot-bands are in general agreement, but line-by-line global production rates show scatter. We now examine several potential causes for this.

A.1. Optical depth effects in the ro-vibrational transitions

The apparent production rate will be reduced when the medium becomes optically thick for ro-vibrational transitions, and this effect may become important close to the nucleus. However, we now show that optical depth effects for ro-vibrational transitions do not affect our derived H_2O rotational temperatures and production rates. We approximate the cometary gas as a population at rest relative to the nucleus (no net outflow) since this represents the worst case (over-estimates the optical depth); velocity dispersion along the line-of-sight leads to reduced optical depths.

In the pump from the ground vibrational level, $\delta_A(\lambda)$ is the optical depth at wavelength λ for absorption of a photon, and can be expressed $\delta_A(\lambda) = K_0 N$, where K_0 is the absorption coefficient at line center (cm^2 molecule^{-1}) and N is the column density of absorbers (molecules cm^{-2}). We assume that opacity effects in the pump dominate (so opacity in the cascade is neglected). The absorption coefficient at line center is (Pugh and Rao, 1976)

$$K_0 = (S_{\mathrm{line}}/\Delta\nu_D)(\ln 2/\pi)^{1/2}, \tag{A.1}$$

where S_{line} is the line strength (cm molecule^{-1}). The Doppler line width ($\Delta\nu_D$, cm^{-1}) is

$$\Delta\nu_D = 3.58 \times 10^{-7}(\nu_0)(T/M)^{1/2}, \tag{A.2}$$

where ν_0 is the line center frequency for the pumping transition (cm^{-1}), T is the gas temperature (K), and M is the molecular weight (g mol^{-1}) of the absorbing gas. The optical depth at line center is defined by the parameter $K_0 N$. A critical column density can be defined by the condition $N_c = K_0^{-1}$ and corresponds to unit optical depth. Measured along the radius vector from the sun to the nucleus, the critical column density is reached at a distance (R_c) from the nucleus. For a spherically symmetric coma with uniform outflow velocity (v_{gas}, cm s^{-1}), R_c can be estimated for each transition (see DiSanti et al., 2001, for additional details):

$$R_c \sim Q/(4\pi v_{\mathrm{gas}} N_c). \tag{A.3}$$

For Ikeya–Zhang, we estimate that even the strongest hot-band lines near 2.9-μm are optically thick only within a few kilometers of the nucleus. Therefore, retrieved fluxes for these lines should not be significantly affected by optical depth, even for nucleus-centered extracts. Lines most severely affected by optical depth are those within the 001–010 hot-band, for which R_c can be as large as a few hundred kilometers in the most severe case. For these lines, we determine production rates using signal from beyond the optically thick region of the coma (from off-nucleus extracts beyond 1.5″), and these lines are not used in the determination of rotational temperature.

A.2. The rotational population distribution in the ground-vibrational level

Since the emitted hot-band lines are optically thin throughout the coma, the population in a respective excited ro-vibrational level can be obtained from the measured line intensity by using the appropriate radiative transition probability. The derived populations show evidence of rotational equilibrium over the regions where production rates and rotational temperatures are calculated (Fig. 6). In forming Fig. 6, we calculated the pumping g-factor for the excited ro-vibrational level using measured line strengths. Downward branching ratios were estimated by adopting the Einstein-A for the corresponding (measured) fundamental band. We also assume that the populations in rotational levels of the ground vibrational state are described by a Boltzmann distribution at a given temperature (Section 4). We now demonstrate that this assumption is likely valid over regions of the coma where production rates and rotational temperatures are determined.

Rotational levels in the ground vibrational state are thermalized only if collisions dominate both excitation and de-excitation of a level, i.e., the collisional excitation rate (C) must exceed the radiative pumping rate and the collisional de-excitation rate (D) must exceed the radiative decay rate (Crovisier and Encrenaz, 1983; Crovisier, 1984; Weaver and

Mumma, 1984). Here we need be concerned only with transitions among rotational levels of the ground vibrational state (000).

For an optically thin coma, the radiative pumping rate is given by the product of the stimulated absorption rate ($B_{\rm lu} g(\nu)\, d\nu$, where $g(\nu)\, d\nu$ is the line-shape function) and the density (ρ_ν) of the radiation field at the position of the molecule, integrated over all frequencies (for a radiation field of uniform density (ρ_o) integral reduces $B_{\rm lu}\rho_o$). If the coma is optically thick, the local radiative pumping term is reduced in size and collisions can control excitation to a greater nucleocentric distance. Likewise, the emitted photon does not escape directly but is scattered instead, increasing the average time spent in the excited rotational level by a factor ($N_{\rm esc}$), reducing the effective radiative transition probability, and permitting collisions to control de-excitation over a larger zone (Crovisier, 1984; Weaver and Mumma, 1984; Bockelée-Morvan, 1987; Xie and Mumma, 1992). For regions in the coma where $A_{\rm ul} > N_{\rm esc} D$, or $B_{\rm lu}\rho > C$ the assumption of a Boltzmann distribution in the ground vibrational level may no longer be valid. However, collisions with electrons may control rotational temperatures in the intermediate coma (Xie and Mumma, 1992).

The collisional excitation rate can be estimated (Xie and Mumma, 1992; see also Crovisier and Encrenaz, 1983; Crovisier and Le Bourlot, 1983; Weaver and Mumma, 1984),

$$C = \left(1.5 \times 10^{-25}\right) Q/r^2. \tag{A.4}$$

The distance from the nucleus (r) is in km, and Q is the total gas production rate (molecules s^{-1}). We note that the estimate for C is highly uncertain largely due to uncertainty in the water-neutral collisional cross-section. For wavelengths smaller than 5-μm, excitation by the direct solar radiation field dominates other excitation mechanisms by orders of magnitude (Crovisier and Encrenaz, 1983; Weaver and Mumma, 1984). Under these conditions the vibrational band g-factor ($g_{\rm band}$) is given by $B_{\rm lu}\rho$ (s^{-1}) (Weaver and Mumma, 1984). The strongest H_2O vibrational band (ν_3) has $g_{\rm band} = 2.67 \times 10^{-4}\ \mathrm{s}^{-1}$. Solving for Eq. (A.4) suggests that $B_{\rm lu}\rho < C$ remains valid out to at least 10^4 km from the nucleus.

The principle of detailed balancing requires that

$$D = C(w_l/w_u)\exp(E_{\rm ul}/kT). \tag{A.5}$$

Where w_u (w_l) is the statistical weight of the upper (lower) level, respectively. Some of the higher energy rotational levels of relevance have large $A_{\rm ul}$, for example, the 101–100 5_{24}–6_{25} line is primarily pumped ($\sim$ 83%) from the 4_{23} ground rotational level, for which the radiative decay rate is $A_{\rm ul} = 0.488\ \mathrm{s}^{-1}$ (for 4_{23}–3_{12}). $E_{\rm ul}$ for 4_{23}–3_{12} is about 127 cm^{-1}, while at 140 (100) K the thermal energy is $\sim$ 100 (70) cm^{-1}. The collisional de-excitation rate is thus larger than the collisional excitation rate by about a factor of 3 (5) in March (April). Evaluating Eqs. (A.4) and (A.5) suggests that within about 900 km ($\sim 1.6''$) of the nucleus in March and about 550 km ($\sim 1.6''$) in April, collisions control the rotational population in this and similar levels. Collisions with electrons could also thermalize rotational levels; it is estimated that the collisional excitation rate for electrons will exceed that of neutrals beyond a few thousand kilometers from the nucleus (Xie and Mumma, 1992).

The foregoing treatment is for rotational transitions that remain optically thin. However, the coma is optically thick to at least some of the rotational transitions. For a comet with gas production rate $= 2 \times 10^{29}$ molecules s^{-1}, some of the low-J rotational transitions are optically thick out to about 10^4–10^5 km from the nucleus under certain conditions (Bockelée-Morvan, 1987). At low inner coma temperatures ($\leqslant$ 50 K), opacity effects for some of the high J transitions of interest to this study (e.g., 4_{23}–3_{12}) are likely unimportant for regions where collisions control the rotational population (in the optically thin case). However, for inner coma temperatures more relevant to Ikeya–Zhang ($\sim$ 100–140 K), the populations of the relevant high J levels will increase significantly. Using Eqs. (A.1)–(A.3) and the rotational line strength for 4_{23}–3_{12}, we estimate for an isothermal coma at 100 K, optical depth $\geqslant 1$ will be maintained for this transition out to a distance of $\sim 1 \times 10^4$ km from the nucleus for the April dates (where $Q_{\rm H_2O} \sim 2 \times 10^{29}$ molecules s^{-1}). For the March dates opacity effects in the rotational transitions will be important out to even larger distances. We note that the coma of Ikeya–Zhang is unlikely to be isothermal. Bockelée-Morvan (1987) studied the effect of opacity on rotational lines assuming non-uniform kinetic temperatures in the coma. The temperature profile for the coma of Ikeya–Zhang is not known, so treatment of opacity effects in a coma with non-uniform temperatures is beyond the scope of this paper.

At these coma temperatures the values of $N_{\rm esc}$ are not known for the transitions relevant for this study, however, opacity in the rotational transitions is significant well outside the region of the coma where collisions control the rotational population in the optically thin case. The net effect of rotational opacity will be an apparent reduction in $A_{\rm ul}$ for the relevant transitions and a significant increase in the distance from the nucleus where collisions can thermalize rotational levels. Beyond a few thousand kilometers, the role of electron collisions becomes increasingly important.

Measurements of fluxes (Table 4) and rotational temperatures based on extracts on and off the nucleus also suggest that the rotational levels are efficiently thermalized within the region of the coma relevant to this study. Rotational temperatures derived from extracts 1.5″–8.5″ off the nucleus agree within error to those derived from on nucleus ($1'' \times 3''$) extracts (e.g., off nucleus extracts derive $T_{\rm rot} \sim 130$ and 90 K with larger error bars than the nucleus-centered extracts for UT March 22.0 and April 13.8). There is no evidence from these data that the approximation of a Boltzmann distribution in the ground vibrational level is invalid over the spatial range of our measurements. If the higher energy levels are

not efficiently thermalized, we expect our derived rotational temperatures and production rates to be underestimated.

A.3. Uncertainties in pump rates and branching ratios

The branching ratios for individual hot-band lines are subject to certain systematic errors, especially the 2.9-μm bands. Values used in the models for the pump rates, vibrational branching ratios and rotational branching ratios between vibrational levels may have significant uncertainties. Errors in pump rates or vibrational branching ratios for a particular band would result in systematically high or low derived values for all lines within that hot-band, however we see no evidence of this (Table 4). We do however see possible evidence of errors in rotational branching ratios (Einstein A's) between vibrational levels, resulting in systematically high or low derived values for individual lines (Table 4, Fig. 6). Such uncertainties are a likely cause for some of the scatter seen in our derived line-by-line production rates.

A.4. Blending with other emissions

We note that several measured emissions represent blends of several unresolved lines (Table 4, Figs. 1, 2). Although it is assumed that all the measured water lines are pure, it is possible that some are blended with unknown emission features. Indeed, spectra in the 2.9-μm region of other comets in our database contain many lines of unknown origin (Dello Russo et al., in preparation). Such blending would cause derived H_2O production rates to be systematically high. Production rates derived for the 101–100 (4_{22}–5_{23}) line are systematically higher than the mean on all three dates it was measured (Table 4), suggesting that this line is blended with an unknown emission feature.

References

A'Hearn, M.F., Schleicher, D.G., Millis, R.L., Feldman, P.D., Thompson, D.T., 1984. Comet Bowell 1980b. Astron. J. 89, 579–591.

Bird, M.K., Janardhan, P., Wilson, T.L., Huchtmeier, W.K., Gensheimer, P., Lemme, C., 1999. K-band radio observations of Comet Hale–Bopp: detections of ammonia and (possibly) water. Earth Moon Planets 78, 21–28.

Biver, N., Rauer, H., Despois, D., Moreno, R., Paubert, G., Bockelée-Morvan, D., Colom, P., Crovisier, J., Gérard, E., Jorda, L., 1996. Substantial outgassing of CO from Comet Hale–Bopp at large heliocentric distance. Nature 380, 137–139.

Biver, N., 13 colleagues, 1999. Spectroscopic monitoring of Comet C/1996 B2 (Hyakutake) with the JCMT and IRAM radio telescopes. Astron. J. 118, 1850–1872.

Biver, N., 22 colleagues, 2002. The 1995–2002 long-term monitoring of Comet C/1995 O1 (Hale–Bopp) at radio wavelength. Earth Moon Planets 90, 5–14.

Bockelée-Morvan, D., 1987. A model for the excitation of water in comets. Astron. Astrophys. 181, 169–181.

Bockelée-Morvan, D., Crovisier, J., 1989. The nature of the 2.8-μm emission feature in cometary spectra. Astron. Astrophys. 216, 278–283.

Brooke, T.Y., Knacke, R.F., Owen, T.C., Tokunaga, A.T., 1989. Spectroscopy of emission features near 3 microns in Comet Wilson (1986l). Astrophys. J. 336, 971–978.

Chiu, K., Neufeld, D.A., Bergin, E.A., Melnick, G.J., Patten, B.M., Wang, Z., Bockelée-Morvan, D., 2001. Post-perihelion SWAS observations of water vapor in the coma of Comet C/1999 H1 (Lee). Icarus 154, 345–349.

Combes, M., 16 colleagues, 1988. The 2.5–12 μm spectrum of Comet Halley from the IKS-VEGA experiment. Icarus 76, 404–436.

Crovisier, J., 1984. The water molecule in comets: fluorescence mechanisms and thermodynamics of the inner coma. Astron. Astrophys. 130, 361–372.

Crovisier, J., 1989. The photodestruction of water in cometary atmospheres. Astron. Astrophys. 213, 459–464.

Crovisier, J., Encrenaz, Th., 1983. Infrared fluorescence of molecules in comets: the general synthetic spectrum. Astron. Astrophys. 126, 170–182.

Crovisier, J., Le Bourlot, J., 1983. Infrared and microwave fluorescence of carbon monoxide in comets. Astron. Astrophys. 123, 61–66.

Crovisier, J., Biver, N., Bockelée-Morvan, D., Colom, P., Jorda, L., Lellouch, E., Paubert, G., Despois, D., 1995. Carbon monoxide outgassing from Comet P/Schwassmann–Wachmann I. Icarus 115, 213–216.

Crovisier, J., Leech, K., Bockelée-Morvan, D., Brooke, T.Y., Hanner, M.S., Altieri, B., Keller, H.U., Lellouch, E., 1997. The spectrum of Comet Hale–Bopp (C/1995 O1) observed with the Infrared Space Observatory at 2.9 astronomical units from the Sun. Science 275, 1904–1907.

Crovisier, J., 11 colleagues, 1999. ISO spectroscopic observations of short-period comets. In: Cox, P., Kessler, M.F. (Eds.), The Universe as Seen by ISO. In: ESA SP, vol. 427. ESA, Nordwijk, pp. 137–140.

Dello Russo, N., DiSanti, M.A., Mumma, M.J., Magee-Sauer, K., Rettig, T.W., 1998. Carbonyl sulfide in Comets C/1996 B2 (Hyakutake) and C/1995 O1 (Hale–Bopp): evidence for an extended source in Hale–Bopp. Icarus 135, 377–388.

Dello Russo, N., Mumma, M.J., DiSanti, M.A., Magee-Sauer, K., Novak, R., Rettig, T.W., 2000. Water production and release in Comet C/1995 O1 Hale–Bopp. Icarus 143, 324–337.

Dello Russo, N., Mumma, M.J., DiSanti, M.A., Magee-Sauer, K., Novak, R., 2001. Ethane production and release in Comet C/1995 O1 Hale–Bopp. Icarus 153, 162–179.

Dello Russo, N., Mumma, M.J., DiSanti, M.A., Magee-Sauer, K., 2002a. Production of ethane and water in Comet C/1996 B2 Hyakutake. J. Geophys. Res. Planets 107 (E11), 5095. 10.1029/2001JE001838.

Dello Russo, N., DiSanti, M.A., Magee-Sauer, K., Gibb, E., Mumma, M.J., 2002b. Production of C_2H_6 and H_2O in Comet 2002 C1 Ikeya–Zhang on one date. In: Warmbein, B. (Ed.), The Proceedings for the Asteroids, Comets, Meteors Conference, Berlin, Germany 2002. In: ESA SP, vol. 500. ESA, Nordwijk, pp. 689–692.

DiSanti, M.A., Mumma, M.J., Dello Russo, N., Magee-Sauer, K., Novak, R., Rettig, T.W., 1999. Identification of two sources of carbon monoxide in Comet Hale–Bopp. Nature 399, 662–665.

DiSanti, M.A., Mumma, M.J., Dello Russo, N., Magee-Sauer, K., Novak, R., Rettig, T.W., 2001. Spatially resolved carbon monoxide emission in Comet Hale–Bopp: production rates and rotational temperatures vs. heliocentric distance. Icarus 153, 361–390.

DiSanti, M.A., Dello Russo, N., Magee-Sauer, K., Gibb, E.L., Reuter, D.C., Mumma, M.J., 2002. CO, H_2CO, and CH_3OH in Comet C/2002 C1 Ikeya–Zhang. In: Warmbein, B. (Ed.), The Proceedings for the Asteroids, Comets, Meteors Conference, Berlin, Germany 2002. In: ESA SP, vol. 500. ESA, Nordwijk, pp. 571–574.

Gibb, E.L., Mumma, M.J., DiSanti, M.A., Dello Russo, N., Magee-Sauer, K., 2002. An infrared search for HDO in comets. In: Warmbein, B. (Ed.), The Proceedings for the Asteroids, Comets, Meteors Conference, Berlin, Germany 2002. In: ESA SP, vol. 500. ESA, Nordwijk, pp. 705–708.

Greene, T.P., Tokunaga, A.T., Toomey, D.W., Carr, J.B., 1993. CSHELL: a high spectral resolution 1–5 μm cryogenic echelle spectrograph for the IRTF. In: Fowler, A.M. (Ed.), Proc. Spie., vol. 1946. pp. 313–324.

Hoban, S., Mumma, M.J., Reuter, D.C., DiSanti, M., Joyce, R.R., 1991. A tentative identification of methanol as the progenitor of the 3.52-μm emission feature in several comets. Icarus 93, 122–134.

Kunde, V.G., Maguire, J.C., 1974. Direct integration transmittance model. J. Quant. Spectrosc. Radiat. Transfer 14, 803–817.

Larson, H.P., Weaver, H.A., Mumma, M.J., Drapatz, S., 1989. Airborne infrared spectroscopy of Comet Wilson 1986l and comparisons with Comet Halley. Astrophys. J. 338, 1106–1114.

Lecacheux, A., 21 colleagues, 2003. Observations of water in comets with Odin. Astron. Astrophys. 402, L55–L58.

Magee-Sauer, K., Mumma, M.J., DiSanti, M.A., Dello Russo, N., Rettig, T.W., 1999. Infrared spectroscopy of the ν_3 band of hydrogen cyanide in C/1995 O1 Hale–Bopp. Icarus 142, 498–508.

Magee-Sauer, K., Mumma, M.J., DiSanti, M.A., Dello Russo, N., Rettig, T.W., Novak, R.E., 2000. Spectroscopy of Comets Lee and LINEAR S4 in the 3 micron region using NIRSPEC. Bull. Am. Astron. Soc. 32, 1075.

Magee-Sauer, K., Mumma, M.J., DiSanti, M.A., Dello Russo, N., 2002a. Hydrogen cyanide in Comet C/1996 B2 Hyakutake. J. Geophys. Res. Planets 107 (E11), 5096. 10.1029/2002JE001863.

Magee-Sauer, K., Dello Russo, N., DiSanti, M.A., Gibb, E., Mumma, M.J., 2002b. Production of HCN and C_2H_2 in Comet C/2002 C1 Ikeya–Zhang on UT April 13.8 2002. In: Warmbein, B. (Ed.), The Proceedings for the Asteroids, Comets, Meteors Conference, Berlin, Germany 2002. In: ESA SP, vol. 500. ESA, Nordwijk, pp. 549–552.

Mumma, M.J., Weaver, H.A., Larson, H.P., Davis, D.S., Williams, M., 1986. Detection of water vapor in Halley's comet. Science 232, 1523–1528.

Mumma, M.J., DiSanti, M.A., Tokunaga, A., Roettger, E.E., 1995. Ground-based detection of water in Comet Shoemaker–Levy 1992 XIX; probing cometary parent molecules by hot-band fluorescence. Bull. Am. Astron. Soc. 27, 1144.

Mumma, M.J., DiSanti, M.A., Dello Russo, N., Fomenkova, M., Magee-Sauer, K., Kaminski, C.D., Xie, D.X., 1996. Detection of abundant ethane and methane, along with carbon monoxide and water, in Comet C/1996 B2 Hyakutake: evidence for interstellar origin. Science 272, 1310–1314.

Mumma, M.J., DiSanti, M.A., Dello Russo, N., Magee-Sauer, K., Rettig, T.W., 2000. Detection of CO and depleted ethane in Comet 21P/Giacobini–Zinner: evidence for variable chemistry in the outer solar nebula. Astrophys. J. 531, L155–L159.

Mumma, M.J., 17 colleagues, 2001a. A survey of organic volatile species in Comet C/1999 H1 (Lee) using NIRSPEC at the Keck Observatory. Astrophys. J. 546, 1183–1193.

Mumma, M.J., Dello Russo, N., DiSanti, M., Magee-Sauer, K., Novak, R.E., Brittain, S., Rettig, T., McLean, I.S., Reuter, D.C., Xu, L.-H., 2001b. The startling organic composition of C/1999 S4 (Linear): a comet formed near Jupiter? Science 292, 1334–1339.

Partridge, H., Schwenke, D.W., 1996. The determination of an accurate isotope dependent potential energy surface for water from extensive ab initio calculations and experimental data. J. Chem. Phys. 106, 4618–4639.

Pugh, L.A., Rao, K.N., 1976. Intensities from infrared spectra. In: Rao, K.N. (Ed.), Molecular Spectroscopy: Modern Research, vol. II. Academic Press, New York, pp. 165–227.

Rothman, L.S., 13 colleagues, 1992. The HITRAN molecular database: editions of 1991 and 1992. J. Quant. Spectrosc. Radiat. Transfer 48, 469–507.

Schermaul, R., Learner, R.C.M., Newnham, D.A., Ballard, J., Zobov, N.F., Belmiloud, D., Tennyson, J., 2001. The water vapor spectrum in the region 8600–15000 cm^{-1}: experimental and theoretical studies for a new spectral line database. II. Line construction. J. Mol. Spectrosc. 208, 43–50.

Schwenke, D.W., Partridge, H., 2000. Convergence testing of the analytic representation of an ab initio dipole moment function for water: improved fitting yields improved intensities. J. Chem. Phys. 113, 6592–6597.

Senay, M.C., Jewitt, D., 1994. Coma formation driven by CO release from Comet Schwassmann–Wachmann I. Nature 371, 229–231.

Shirin, S.V., Polyansky, O.L., Zobov, N.F., Barletta, P., Tennyson, J., 2003. Spectroscopically determined potential energy surface of $H_2{}^{16}O$ up to 25000 cm^{-1}. J. Chem. Phys. 118, 2124–2129.

Tennyson, J., Zobov, N.F., Williamson, R., Polyansky, O.L., Bernath, P.F., 2001. Experimental energy levels of the water molecule. J. Phys. Chem. Ref. Data 30, 735–831.

Tennyson, J., Kostin, M.A., Barletta, P., Harris, G.J., Ramanlal, J., Polyansky, O.L., Zobov, N.F., 2003. DVR3D: a program suite for the calculation of rotational–vibrational spectra of triatomic molecules. Computer Phys. Comm. In press.

Tokunaga, A.T., Nagata, T., Smith, R.G., 1987. Detection of a new emission band at 2.8 microns in Comet P/Halley. Astron. Astrophys. 187, 519–522.

Weaver, H.A., Mumma, M.J., 1984. Infrared molecular emissions from comets. Astrophys. J. 276, 782–797.

Weaver, H.A., Mumma, M.J., Larson, H.P., Davis, D.S., 1986. Post-perihelion observations of water in Comet Halley. Nature 324, 441–446.

Weaver, H.A., Brooke, T.Y., Chin, G., Kim, S.J., Bockelée-Morvan, D., Davies, J.K., 1999a. Infrared spectroscopy of Comet Hale–Bopp. Earth Moon Planets 78, 71–80.

Weaver, H.A., Chin, G., Bockelée-Morvan, D., Crovisier, J., Brooke, T.Y., Cruikshank, D.P., Geballe, T.R., Kim, S.J., Meier, R., 1999b. An infrared investigation of volatiles in Comet 21P/Giacobini–Zinner. Icarus 142, 482–497.

Xie, X., Mumma, M.J., 1992. The effect of electron collisions on rotational populations of cometary water. Astrophys. J. 386, 720–728.

Xie, X., Mumma, M.J., 1996. Monte Carlo simulation of cometary atmospheres: application to Comet P/Halley at the time of the Giotto spacecraft encounter. II. Axisymmetric model. Astrophys. J. 464, 457–475.

Zobov, N.F., Polyansky, O.L., Tennyson, J., Shirin, S.V., Nassar, R., Hirao, T., Imajo, T., Bernath, P.F., Wallace, L., 2000. Using laboratory spectroscopy to identify lines in the K- and L-band spectrum of water in a sunspot. Astrophys. J. 530, 994–998.